Influences of flow direction, temperature and relative humidity on the performance of a representative Anion Exchange Membrane Fuel Cell: A Computational Analysis

Bruno S. Machado [1,✉], Nilanjan Chakraborty [1], Prodip K. Das [1]

[1]School of Mechanical and Systems Engineering, Newcastle University, Newcastle-Upon-Tyne, NE1 7RU, UK

✉Corresponding author.

B.De-Souza-Machado1@newcastle.ac.uk

NOMENCLATURE

a	water activity	Greek letters	
A	active reaction area, m^2	α	transfer coefficient
A_S	specific reactive surface area, $m^2\ m^{-3}$	γ	water phase change rate, s^{-1}
C	molar concentration, kmol m^{-3}	ϵ	porosity
C_P	specific heat, J $kg^{-1}\ K^{-1}$	ζ	water transfer rate, s^{-1}
D	mass diffusivity, $m^2\ s^{-1}$	η	overpotential, V
E	total energy in the gaseous phase, J	θ	contact angle, °
EW	equivalent molecular weight of dry membrane, kg $kmol^{-1}$	κ	electrical conductivity, S m^{-1}
F	Faraday's constant, C $kmol^{-1}$	λ	membrane water content
G	Gibbs free energy, J mol^{-1}	$\emptyset$	non-dimensional minimum cell distance
h	latent heat, J kg^{-1}	μ	dynamic viscosity, kg $m^{-1}\ s^{-1}$
I	current density, A m^{-2}	ξ	stoichiometry ratio
j	reaction rate, A m^{-3}	ρ	density, kg m^{-3}
j_0	exchange current density, A m^{-2}	σ	surface tension, N m^{-1}
k	thermal conductivity, W $m^{-1}\ kg^{-1}$	ϕ	electronic potential
K	permeability, m^2	ω	ionomer volume fraction
L	largest dimension in the direction in question, m	Δ	cell size in the direction in question, m
$\dot{m}$	mass flow rate, kg s^{-1}	$\bar{\bar{\tau}}$	viscous stress tensor, Pa
M	molecular weight, kg $kmol^{-1}$	Subscript and Superscript	
$\vec{N}$	diffusion flux of species, $m^2\ s^{-1}$	a	anode
n_d	electro osmotic drag coefficient	BP	bipolar plate
P	pressure, Pa	CL	catalyst layer
R	universal gas constant, J $kmol^{-1}\ K^{-1}$	c	cathode, capillary
RH	relative humidity	cell	cell
s	liquid water fraction	cond	condensation
T	temperature, K	d	dissolved
T_0	operating temperature, K	S	source terms, entropy, J $kmol^{-1}\ K^{-1}$
$\vec{u}$	superficial velocity vector, m s^{-1}	eff	effective
$\vec{U}$	physical velocity vector, m s^{-1}	e	equilibrium
V	Potential, V	evap	evaporation
X	mole fraction	GDL	gas diffusion layer
Y	mass fraction	g	gas phase

H_2	hydrogen
0	intrinsic value
l	liquid phase
mem	mass, membrane
min	minumum
m	membrane phase
u	momentum
out	output
O_2	oxygen
ref	reference
rev	reversible
sat	saturation
s	solid phase
i	species
v-l	vapour to liquid (vice-versa)
H_2O	water
w	water vapour phase

ABSTRACT

In this study, a three-dimensional Computational Fluid Dynamic model for a typical Anion Exchange Membrane (AEM) fuel cell was developed and used to analyse the influence of the flow direction in anode and cathode channels on the overall fuel cell performance. In the co-flow configuration, both anode and cathode inlets are located at the same side, whereas in the counter-flow configuration the cathode inlet is located in the opposite side to the anode inlet. In addition to the comparison of flow mode, the overall performance of the fuel cell for a counter-flow configuration is evaluated for different operating temperature and the relative humidity values in the flow channel inlet. The comparison of polarisation curves for different flow modes exhibited no significant influence on the overall performance for the parameters used in this study. Nevertheless, the variation of the operating parameters have been shown to affect the overall performance of the fuel cell significantly in the counter-flow mode. As the temperature rose, the electrochemical kinetics were enhanced and diffusion of ions was also facilitated due to a better hydration environment, resulting in a better overall performance. On the other hand, a poorly hydrated membrane was obtained when the relative humidity was decreased due to a smaller extent of back diffusion of water from the anode catalyst layer to the cathode catalyst layer and consequently, the diffusion of ions was negatively affected.

Keywords: Anion exchange membrane, co-flow, counter-flow, relative humidity, temperature.

1. INTRODUCTION

The global demand for alternative sources of energy has increased considerably in the past few decades. Thus, extensive effort has been directed to the electrochemical energy conversion and storage technologies, such as batteries, super-capacitors, fuel cells to name a few. In the respect of energy conversion, several kinds of fuel cells have been developed such as polymer exchange membrane fuel cell (PEMFC), solid oxide fuel cell (SOFC) and direct methanol fuel cell (DMFC) to name a few major categories. High efficiency compared to conventional fossil fuel fired engines, high power density and the absence of greenhouse gas emission are just some of the advantages of the PEMFC compared to fossil fuel engines [1, 2]. Moreover, the applications of PEMFC include but not limited to electronic devices, transportation and stationary generators. In order to make PEMFCs a feasible alternative to energy conversion, the main challenge, in terms of material, lies in the production of a membrane with the following characteristics: low cost, high ion conductivity, satisfactory mechanical properties and durability [3-6]. The PEMFCs can be classified in proton exchange membrane (PEM) and anion exchange membrane (AEM), and their schematic representations are shown in Figure 1.

The complexities and uncertainties of the first has been widely analysed in the recent literature and mathematical analysis and numerical modelling are becoming increasingly essential to gain fundamental insights into the heat, momentum and species transport phenomena within fuel cells [7-13]. To date, limited effort have been directed to the numerical modelling of underlying electrochemical and transport phenomena presented in the energy conversion in AEM fuel cells [14-16], and the present analysis addresses this gap in existing literature.

The general representation of the electrochemical reaction in an AEM fuel cell is presented below:

$$Anode: H_2 + 2OH^- \rightarrow 2H_2O + 2e^- \quad (1)$$

$$Cathode: H_2O + 2e^- + \frac{1}{2}O_2 \rightarrow 2OH^- \quad (2)$$

$$Overall: H_2 + \frac{1}{2}O_2 \rightarrow H_2O + heat\ generation + electrical\ energy \quad (3)$$

It is worth noting that water, the product of the electrochemical reaction, plays a crucial role in determining the overall efficiency of the fuel cell. When in abundance, the water can flood the catalyst layers and limit the transport of reactants within the layer [7, 17]. On the other hand, the humidification

of the membrane has a positive effect on the ion transportation through the catalyst layers and membrane [18]. The catalyst layer is often modified in order to optimise the overall efficiency of the fuel cell [19-21]. Results suggested that the optimum ionomer content in the catalyst layer varies depending on the temperature, as it has dependence on the balance between the OH^- ion/water mobility and the oxygen solubility [22, 23]. In addition, the catalyst layer structure and wettability influence the liquid-water transport within the cell, which can further change the hydration of the membrane and the optimum ionomer content [8]. Another analysis [24] focused on the oxygen reduction in a Co based cathode catalyst layer, where the performance in alkaline AEM fuel cell is comparable with one with Pt in its base. A high-fidelity numerical model can potentially play a complementary role to experimental investigations, and can provide detailed insights into the interactions between the electrochemical mechanism, and heat and mass transport phenomena, which play pivotal roles in water management of AEM fuel cells. One-dimensional numerical analyses conducted by Sohn *et al.* [25] reinforced the importance of the anode humidification in order to achieve better membrane performance. Results suggested that under dry anode condition, the overall fuel cell performance was significantly negatively affected [25]. Numerical and experimental analyses were conducted in order to evaluate the deviated concentration loss in alkaline AEM fuel cells [26]. Results suggested that charge transfer and anion transport resistances negatively affect the fuel cell performance above a threshold current density, and better cathode catalyst layer hydration and overall performance can be obtained as a result of judicious water management [26]. Three-dimensional numerical analyses of water transport, production and phase change have been reported in the literature on PEM fuel cells [27, 28], whereas water management models were considered only on the anode side for AEM fuel cells [16]. With respect to the flow mode, PEM fuel cells have been numerically analysed for both co-flow and counter-flow (where the flow direction in the cathode side was inverted in comparison to the anode side) configurations [29]. Subsequently a transient analysis has been performed in order to analyse the dynamic effects of operating parameters on the anode side in the AEM fuel cells [14]. Jiao et al. [15] proposed a comprehensive three-dimensional steady state numerical model for a single-channel AEM fuel cell and numerical results exhibited reasonable agreement with experimental results [15]. Further analyses [30] on the water transport in alkaline AEM fuel cell have been carried where the interfacial

effect has also been taken into account. Deng *et al.* [30] suggested that membrane thickness, micro porous layers (MPL) in the anode side and pressure at the anode side have significant influences on the overall performance of the alkaline AEM fuel cell, as they affect the water transport through the membrane. Experimental [31] and numerical [30] analyses on the use of MPL and the effect of electrode characteristics in alkaline AEM fuel cell have also been carried out. It has been observed that the use of MPL and increasing the back pressure on the anode side contribute to the enhancement of the fuel cell performance [30]. However, the lack of water supply on the cathode side is still an issue to be addressed [32]. The numerical optimization of an alkaline membrane fuel cell was proposed by Sommer *et al.* [33], where three degrees of freedom were considered. For the cases studied, Sommer *et al.* [33] observed a 600% variation in the net power output of the fuel cell, clearly demonstrating the importance of well dimensioned components on the performance. Nevertheless, the effects of flow direction in the channels for both anode and cathode are yet to be analysed in detail for AEM fuel cells. The aim of this work is to develop a steady state three-dimensional AEM fuel cell model, which is capable of reproducing the electrochemistry within the catalyst layers and accounting for the water transport, production and phase change within typical AEM fuel cells.

In this study, a three-dimensional representative model of an AEM fuel cell is proposed, and the effects of temperature, relative humidity and flow direction in anode and cathode channels on the overall performance of the fuel cell have been investigated.

2. MATHEMATICAL BACKGROUND

2.1 Assumptions

For the purpose of the computational economy, a number of assumptions have been made in this numerical investigation. Here a steady-state model is considered without the presence of body forces (e.g. gravity). The contamination of gases at the channel inlet is neglected and the gaseous species are considered to be ideal gases. The gas flow within the channel is considered to be laminar (because the Reynolds number in the channel remains of the order of 10^2 based on hydraulic diameter) and no liquid

water presence is assumed in the flow channel. The membrane is considered to be impermeable and thus the species cannot cross it.

2.2 Mathematical framework

2.2.1 Transport equations of gas mixture

The transports of gas mixture in the flow channel, catalyst layer and, gas diffusion layer are governed by the mass, momentum and species conservation equation. The mass conservation equation can be given as:

$$\nabla \cdot \left(\rho_g \vec{u}_g\right) = S_m \tag{4}$$

where ρ_g is the density of the gaseous phase and $\vec{u}_g$ is the superficial velocity vector, which is proportional to the physical velocity vector $\vec{U}$, as given below:

$$\vec{u}_g = \epsilon(1-s)\vec{U} \tag{5}$$

where ϵ is the porosity in the domain and s is the volume fraction of the liquid water occupied in the void. The source term of the mass conservation equation, S_m, is defined as

$$S_m = S_{H_2} + S_{O_2} + S_{H_2O} \tag{6}$$

where S_{H_2}, S_{O_2} and S_{H_2O} are the species source terms, and they will be defined later.

The momentum equation under steady-state takes the following form:

$$\nabla \cdot \left(\frac{1}{\left(\epsilon(1-s)\right)^2}\rho_g \vec{u}_g \vec{u}_g\right) = -\nabla P_g + \nabla \cdot (\bar{\bar{\tau}}) + S_u \tag{7}$$

where P_g is the pressure field of the gaseous phase, $\bar{\bar{\tau}}$ is the viscous stress tensor. The Darcy's Law is used to describe the flow of the gaseous phase through the porous medium, thus, the source term of the momentum equation is defined as:

$$S_u = \begin{cases} -\frac{\mu_g}{K_g}\vec{u}_g \text{ (in CL and GDL)} \\ 0.0 \text{ (in other domains)} \end{cases} \tag{8}$$

where μ_g and K_g stand for the dynamic viscosity and the effective permeability of the gas in the porous medium. As the permeability of the liquid and gaseous phase are affected by the saturated water in the porous medium, the effective permeability for gaseous and liquid phase (K_g and K_l) are given as [14]:

$$K_g = K_0(1-s)^{4.0} \tag{9}$$

$$K_l = K_0 s^{4.0} \tag{10}$$

where K_0 is the intrinsic permeability of the medium.

The species conservation equation can be given as:

$$\nabla \cdot \left(\rho_g \vec{u}_g Y_i\right) = \nabla \cdot \left(\rho_g D_i^{eff} \nabla Y_i\right) + S_i \tag{11}$$

where i denote the gas species, Y_i is the mass fraction, D_i^{eff} is the effective diffusivity and S_i is the source term of the i^{th} species. Due to the porosity and the volume occupied by the liquid water in the porous medium, the species diffusivity has to be corrected. Thus, the corrected diffusivity for the i^{th} species is estimated using the Bruggeman approximation [34, 35]:

$$D_i^{eff} = D_i \epsilon^{1.5}(1-s)^{1.5} \tag{12}$$

where D_i is the mass diffusivity for the ith species, listed in the Table 1. The source term for different species is defined as:

$$S_{H_2} = \begin{cases} -\frac{j_a}{2F} M_{H_2} & \text{(in anode CL)} \\ 0.0 & \text{(in other domains)} \end{cases} \tag{13}$$

$$S_{O_2} = \begin{cases} -\frac{j_c}{4F} M_{O_2} & \text{(in cathode CL)} \\ 0.0 & \text{(in other domains)} \end{cases} \tag{14}$$

$$S_{H_2O} = \begin{cases} -S_{v-l} & \text{(in anode CL)} \\ -\frac{j_c}{2F} M_{H_2O} + S_{mem} M_{H_2O} \frac{\rho_{mem}}{EW} & \text{(in cathode CL)} \\ -S_{v-l} & \text{(in anode GDL)} \\ 0.0 & \text{(in other domains)} \end{cases} \tag{15}$$

where the subscripts a and c denote anode and cathode, respectively, j is the local current density, M_i is the molecular weight of the i^{th} species, F is the Faraday constant (96487000 C/kmol) and the

remaining terms are the source terms regarding the liquid and dissolved phase and further explanation will be presented later.

The local current density for the anode and cathode side, defined by the Butler-Volmer equation [15], can be expressed as:

$$j_a = (1-s)A_s j_{0,a}\left(\frac{C_{H_2}}{C_{H_2}^{ref}}\right)^{0.5}\left[\exp\left(\frac{\alpha_a n_a F}{RT}\eta\right) - \exp\left(\frac{(1-\alpha_a)n_a F}{RT}\eta\right)\right] \quad (16)$$

$$j_c = A_s j_{0,c}\left(\frac{C_{O_2}}{C_{O_2}^{ref}}\right)\left[\exp\left(\frac{\alpha_c n_c F}{RT}\eta\right) - \exp\left(\frac{(1-\alpha_c)n_c F}{RT}\eta\right)\right] \quad (17)$$

where A_s is the specific reactive surface area; C_{H_2} and C_{O_2} are the molar concentration for the hydrogen and oxygen, respectively; $C_{H_2}^{ref}$ and $C_{O_2}^{ref}$ are the reference molar concentration of hydrogen and oxygen, respectively; A_s is the specific area of the catalyst layer; $j_{0,a}$ and $j_{0,c}$ are the exchange current density at the anode and cathode side, respectively; α_a and α_c are the anodic and cathodic charge transfer coefficient, respectively; R is the universal gas constant (8314 J/kmolK); T is the absolute temperature in K and η is the overpotential. In this study, the overpotential is defined as follows:

$$\eta = \phi_s - \phi_m \quad (18)$$

where ϕ_s and ϕ_m are the electronic and ionic potential, respectively. The electrochemical kinetics parameters are presented in the Table 2 according to Ref. [36].

2.2.2 Transport of liquid water

The continuity equation for the liquid water fraction is described as:

$$\nabla \cdot (\rho_l \vec{u}_l) = S_l \quad (19)$$

where ρ_l is the liquid water density. The liquid water transport inside the fuel cell is driven by the capillary pressure, P_c, and which is expressed as [7]:

$$P_c = P_l - P_g = f(s) \quad (20)$$

where P_g and P_l are the gaseous and liquid pressure, respectively, and they are related with the liquid water fraction. According to Darcy's law one gets:

$$\vec{u}_g = -\frac{K_g}{\mu_g}\nabla \mathrm{P_g} \tag{21}$$

$$\vec{u}_l = -\frac{K_l}{\mu_l}\nabla \mathrm{P_l} \tag{22}$$

where μ_l is the liquid water dynamic viscosity. Then, rearranging the Eqs. 21 and 22 into Eq. 20, yields

$$\vec{u}_l = -\frac{K_l}{\mu_l}\nabla P_c + \frac{K_l}{\mu_l}\nabla P_g \tag{23}$$

Since the capillary pressure is dependent on the liquid fraction, one gets:

$$\nabla P_c = \frac{dP_c}{ds}\nabla s \tag{24}$$

Thus, the liquid water conservation equation can be rewritten as [28]:

$$\nabla \cdot \left(-\frac{\rho_l K_l}{\mu_l}\frac{dP_c}{ds}\right)\nabla s + \nabla \cdot \frac{\rho_l \mu_g K_l}{\mu_l K_g}\vec{u}_g = S_l \tag{25}$$

The capillary pressure, according to the Leverett-J function [7, 37], is expressed as:

$$P_c = \begin{cases} \sigma \cos\theta \left(\frac{\epsilon}{K_0}\right)^{0.5} [1.42(1-s) - 2.12(1-s)^2 + 1.26(1-s)^3] & \text{if } \theta \le 90° \\ \sigma \cos\theta \left(\frac{\epsilon}{K_0}\right)^{0.5} [1.42s - 2.12s^2 + 1.26s^3] & \text{if } \theta > 90° \end{cases} \tag{26}$$

where σ is the surface tension coefficient and θ is the contact angle. It is worthwhile to note that the capillary pressure (P_c) and related wetting properties (such are breakthrough pressure and adhesion force) of porous transport layers (GDL and catalyst layer) are functions of contact angle, pore size, pore structure, and the thickness of the layer [38-40]. These wetting properties influence the capillary pressure and hence the liquid droplet formation and detachment. In the present study, the effects of liquid-water droplet formation and detachment on the performance of the cell have been neglected. Since the Leverett-J function has been widely used for fuel cell models and it provides a reasonable estimation of capillary pressure for any arbitrary porous transport layers with a known contact angle [7, 41], this approach has been adopted for the current analysis. However, the present model is capable of incorporating the experimentally measured capillary pressure and related wetting properties values, which would be addressed in the future investigations. Inside the porous medium at the anode catalyst and gas diffusion layer, the difference between water gaseous phase and saturated pressure raises the possibility of evaporation and condensation phenomena. This is accounted for as [42]:

$$S_{v-l} = \begin{cases} \gamma_{cond}\epsilon(1-s)\frac{M_{H_2O}}{RT}\left(P_{H_2O} - P_{sat}\right) & \text{if } P_{H_2O} \geq P_{sat} \\ \gamma_{evap}\epsilon s\frac{M_{H_2O}}{RT}\left(P_{H_2O} - P_{sat}\right) & \text{if } P_{H_2O} < P_{sat} \end{cases} \quad (27)$$

where γ_{cond} and γ_{evap} are the condensation and evaporation rates, respectively; P_{H_2O} and P_{sat} are the water gaseous phase pressure and the saturation pressure, respectively. The saturation pressure is obtained using the following empirical expression [43]:

$$\log_{10}\left(\frac{P_{sat}}{101325}\right) = -2.1794 + 0.02953(T - 273.15) - 9.1837\text{x}10^{-5}(T - 273.15)^2 + 1.4454\text{x}10^{-7}(T - 273.15)^3 \quad (28)$$

The water produced as the product of the electrochemical reaction at the anode catalyst layer is considered to be in the liquid phase, thus, the source term of the liquid water conservation equation is given by:

$$S_l = \begin{cases} \frac{j_a}{F}M_{H_2O} + S_{v-l} + S_{mem}M_{H_2O}\frac{\rho_{mem}}{EW} & \text{(in anode CL)} \\ S_{v-l} & \text{(in anode GDL)} \end{cases} \quad (29)$$

2.2.3 Membrane water content

Due to the forward and backward diffusion, and also for the electro-osmotic drag, water is transported through the membrane. This is accounted for by the membrane water content. The transport equation of membrane water content is given as [28]:

$$-\nabla\cdot\left(D_d^{eff}\nabla\lambda\right) + \nabla\cdot\left(\frac{EW}{\rho_{mem}}\frac{n_d}{F}\vec{J}_m\right) = S_d \quad (30)$$

where D_d is the diffusivity of the membrane water content, EW is the equivalent molecular weight of the membrane in a dry condition, ρ_{mem} is the membrane density. The membrane water content can be related to the dissolved water concentration by the following expression:

$$\lambda = \frac{EW}{\rho_{mem}}C_d \quad (31)$$

where C_d is the dissolved water molar concentration. The diffusion coefficient of water membrane content is calculated as [16]:

$$D_d = \begin{cases} (0.0051\lambda T_0 - 1.44\lambda)\text{x}10^{-10} & 0.0 \leq \lambda \leq 14.0 \\ \left[(-23.2404 + 4.513\lambda - 0.28926\lambda^2 + 0.006131\lambda^3)(T_0 - 303.15) \right. & \\ \left. -79.826 + 17.928\lambda - 1.3329\lambda^2 + 0.03337\lambda^3\right]\times 10^{-10} & 14.0 < \lambda \leq 19.0 \\ [(-41.916 + 0.00613\lambda^3)(T_0 - 303.15) + 8.5139]\text{x}10^{-10} & \lambda > 19.0 \end{cases} \quad (32)$$

Nevertheless, due to the ionomer content in the catalyst layer, the membrane water content diffusivity coefficient has to be corrected as:

$$D_d^{eff} = \omega^{1.5} D_d \tag{33}$$

where ω is the volume fraction of the ionomer in the catalyst layer. The electro-osmotic drag coefficient, n_d, is expressed as [43]:

$$n_d = \frac{2.5}{22}\lambda \tag{34}$$

The water flux in and out of the membrane due to the sorption and desorption is defined in an equilibrium approach in the following manner [27]:

$$S_{mem} = \zeta_{mem}(\lambda_e - \lambda) \tag{35}$$

where ζ_{mem} is the water transfer rate and λ_e is the membrane water content in an equilibrium hydration state and it can be computed as [15]:

$$\lambda_e = \begin{cases} (-0.605a^3 + 0.85a^2 - 0.205a + 0.153)(T_0 - 313.15) + 39.0a^3 - 47.7a^2 + 23.4a + 0.117 & 0 \le a \le 1.0 \\ (-0.00265a + 0.05795)(T_0 - 313.15) + 1.5915(a - 1) + 14.817 & 1.0 < a \le 3.0 \end{cases} \tag{36}$$

where a is the water activity, which is defined as:

$$a = \frac{X_{H_2O} P_g}{P_{sat}} + 2s \tag{37}$$

The source term of the membrane water content transport equation is defined as:

$$S_d = \begin{cases} -S_{mem} & \text{(in anode CL)} \\ -S_{mem} & \text{(in cathode CL)} \end{cases} \tag{38}$$

2.2.4 Electrical potential

The electronic and ionic potential fields are governed by the Ohm's Law, and they can be expressed, respectively, as [44]:

$$-\nabla \cdot \left(\kappa_s^{eff} \nabla \phi_s\right) = -\nabla \cdot \left(\vec{J}_s\right) = S_s \tag{39}$$

$$-\nabla \cdot \left(\kappa_m^{eff} \nabla \phi_m\right) = -\nabla \cdot \left(\vec{J}_m\right) = S_m \tag{40}$$

where κ_s^{eff} and κ_m^{eff} are the effective conductivity of electrons and ions, respectively; $\vec{J}_s$ and $\vec{J}_m$ are the electronic and ionic current density, respectively; S_s and S_m are the source term for the electronic and ionic potential conservation equations, respectively. The conductivities are dependent on the physical

properties of the medium, which are evaluated using the Bruggeman approximation and the expressions are given as [34, 35]:

$$\kappa_s^{eff} = (1 - \epsilon - \omega)^{1.5}\kappa_s \tag{41}$$

$$\kappa_m^{eff} = \omega^{1.5}\kappa_m \tag{42}$$

where ω is the ionomer volume fraction and κ_s and κ_m are the electronic and ionic conductivity, respectively. Nevertheless, the ionic conductivity is dependent on the operating temperature and also the water activity in the vapour phase, as presented in the following expression [15]:

$$\begin{aligned} a_w = {} & 0.8118 - 2.296\text{x}10^{-3}T_0 + (5.815\text{x}10^{-3}T_0 - 2.005)\lambda - (2.977\text{x}10^{-3}T_0 - 1.046)\lambda^2 \\ & + (4.825\text{x}10^{-4}T_0 - 0.1676)\lambda^3 - (3.179\text{x}10^{-5}T_0 - 0.01094)\lambda^4 \\ & + (7.427\text{x}10^{-7}T_0 - 2.539\text{x}10^{-4})\lambda^5 \end{aligned} \tag{43}$$

$$\begin{aligned} \kappa_m = {} & 0.1334 - 3.882\text{x}10^{-4}T_0 + (0.01148T_0 - 3.909)a_w - (0.06690T_0 - 23.01)a_w^2 \\ & + (0.1227T_0 - 42.61)a_w^3 - (0.06021T_0 - 21.80)a_w^4 \end{aligned} \tag{44}$$

where a_w is the water activity in the vapour phase. The electrons and ions generated through the electrochemical reaction are accounted for by the source terms in Eqs. 39 and 40, and are expressed as:

$$S_S = \begin{cases} j_a \text{ (in anode CL)} \\ -j_c \text{ (in cathode CL)} \\ 0.0 \text{ (in other domains)} \end{cases} \tag{45}$$

$$S_m = \begin{cases} -j_a \text{ (in anode CL)} \\ j_c \text{ (in cathode CL)} \\ 0.0 \text{ (in other domains)} \end{cases} \tag{46}$$

2.2.5 Energy equation

The energy conservation equation for a multi-phase flow in porous media, multi-species model can be expressed as:

$$\nabla \cdot \left(\vec{u}_g\left(\rho_g E_g + P_g\right)\right) = \nabla \cdot \left(k^{eff}\nabla T - \left(\sum_i h_i \vec{N}_i\right) + \left(\bar{\bar{\tau}} \cdot \vec{u}_g\right)\right) + S_T \tag{47}$$

where k^{eff} is the effective conductivity, E_g is the total energy in the gaseous phase, h_i is the sensible enthalpy for the i^{th} species, $\vec{N}_i$ is the diffusion flux of the species i. Further explanation of the energy conservation equation can be found elsewhere [45]. The source of heat, S_T, is composed by the

reversible heat released during the electrochemical reaction, the irreversible heat, the ohmic heat and the latent heat during the water phase change and sorption/desorption process. Thus, the heat source term for the different domains is defined as [46]:

$$S_E = \begin{cases} j_a\left(\frac{j_a T\Delta S}{2F} + |\eta|\right) + \|\nabla\phi_s\|^2\kappa_S^{eff} + \|\nabla\phi_m\|^2\kappa_m^{eff} + h_{cond}\left(S_{v-l} - \frac{\rho_{mem}}{EW}M_{H_2O}S_{mem}\right) \text{ (in anode CL)} \\ j_c|\eta| + \|\nabla\phi_s\|^2\kappa_S^{eff} + \|\nabla\phi_m\|^2\kappa_m^{eff} + h_{cond}\left(S_{v-l} - \frac{\rho_{mem}}{EW}M_{H_2O}S_{mem}\right) \text{ (in cathode CL)} \\ \|\nabla\phi_s\|^2\kappa_S^{eff} + h_{cond}S_{v-l} \text{ (in GDL)} \\ \|\nabla\phi_s\|^2\kappa_S^{eff} \text{ (in BP)} \\ \|\nabla\phi_m\|^2\kappa_m^{eff} \text{ (in membrane)} \\ 0.0 \text{ (in other domains)} \end{cases} \quad (48)$$

where ΔS is the entropy change of the HOR.

2.3 Boundary Condition

In this study, the mass flow rates at the anode and cathode inlets, respectively, are specified as:

$$\dot{m}_a = \frac{\rho_g^a \xi_a I_{ref} A}{2F C_{H_2}} \quad (49)$$

$$\dot{m}_c = \frac{\rho_g^c \xi_c I_{ref} A}{4F C_{O_2}} \quad (50)$$

where ξ_a and ξ_c are the stoichiometry ratios of anode and cathode, respectively; I_{ref} is the reference current density; A is the active reaction area; ρ_g^a and ρ_g^c are the density of the gas mixture at the anode and cathode, inlet respectively. The hydrogen and oxygen concentration at the anode and cathode inlet are specified as:

$$C_{H_2} = \frac{(P_a - RH\ P_{sat})}{RT_0} \quad (51)$$

$$C_{O_2} = \frac{0.21(P_c - RH\ P_{sat})}{RT_0} \quad (52)$$

where P_a and P_c are the inlet pressure at the anode and cathode, RH is the relativity humidity at the inlet. In the oxygen concentration at the cathode inlet, 0.21 represents the molar fraction of oxygen provided in the air mixture. The operating temperature, T_0, is also specified at both anode and cathode inlets.

The approach suggested by Hao *et al.* [28] is used to specify the electronic potential boundary conditions. Thus, the boundary condition of the electronic potential is specified at the top surface of the anode and at the bottom surface of the cathode electrode as:

$$\phi_S^a = V_{rev} - V_{out} \tag{53}$$

$$\phi_S^c = 0.0 \tag{54}$$

where V_{rev} is the theoretical reversible voltage and V_{out} is the output voltage. Considering a thermodynamic equilibrium state, the theoretical reversible energy can be written in a modified version of the Nernst equation as:

$$V_{rev} = \frac{\Delta G_{ref}}{2F} + \frac{\Delta S_{ref}}{2F}\left(T - T_{ref}\right) + \frac{RT}{2F}\ln\left[\left(\frac{P_{H_2}}{P_{ref}}\right)\left(\frac{P_{O_2}}{P_{ref}}\right)^{1/2}\right] \tag{55}$$

where ΔG_{ref} is the Gibbs free energy change, ΔS_{ref} is the entropy change at reference temperature and pressure, T_{ref} and P_{ref}, respectively, P_{H_2} is the partial hydrogen pressure, P_{O_2} is the partial oxygen pressure. The Neumann condition (symmetry or no-flux condition) is applied for all other boundary conditions, which is given by:

$$\frac{\partial \varphi}{\partial n} = 0.0 \tag{56}$$

where φ can be any variable of interest.

2.4 Computational domain

For the purpose of the computational economy, a straight channel half-cell is considered. The computational domain is shown in Fig. 2. The relevant structural parameters and physical properties are presented in the Table 3 and Table 4 [15, 36], respectively.

2.5 Numerical procedure

All the conservation equations are solved in a coupled manner in the framework of the finite-volume method using a commercial software package ANSYS FLUENT. The implementation of the scalar equations and auxiliary functions was carried out through the user defined functions (UDF). A second-order central difference scheme is used for the diffusive term, whereas a second–order upwind scheme is used for convective terms. The well-known SIMPLE algorithm [47] is used for linking the pressure

and velocity fields. The convergence criterion of 5×10^{-7} for the normalised residuals does has been considered and it has been ensured that a smaller value of normalised residual does not significantly affect the results. An extensive grid independence analysis has been carried out using nine different Cartesian meshes, which are referred to as M1 to M9, with non-uniform grid spacing. The non-dimensional minimum cell distance and the grid expansion ratio values are presented in Table 5, where N^x , N^y and N^z are the number of grid points in the x, y and z directions and Err^x, Err^y and Err^z are the associated errors with respect of the variation of the number of grid points in x, y and z directions, respectively. The following equation defines the error associated to the variation of the number of grid points in the y direction, but a similar approach was also extended to other directions:

$$Err^y = \left| \frac{J_{N^{ref,y}} - J_{N^y}}{J_{N^{ref,y}}} \right| \tag{57}$$

where $J_{N^{ref,y}}$ is the mean current density for the reference mesh in the y direction. It was observed that the mesh density in x and z directions do not significantly affect the computational results, whereas the error associated with number of volumes in the y direction is sensitive to the mesh density in this direction. Thus, M5 has been considered for the current analysis for the purpose of computational economy and the total error, Err, associated with it can be estimated as:

$$Err \leq \sqrt{|Err^x|^2 + |Err^y|^2 + |Err^z|^2} = 4.49\% \tag{58}$$

The numerical model is validated by comparing the polarization curve (i.e. variation of voltage with current density) obtained from numerical simulations with experimental findings [48], as shown in the Figure 3, which reveals that a good agreement is achieved between numerical and experimental findings. However, some parameters (e.g. kinetic parameters, porosity, and intrinsic permeability) were not specified in Ref. [48] and typical values for these quantities (see Tables 2 and 3) are chosen for numerical simulations. An almost constant parallel shift between the voltage-current density characteristics between experimental and computation results indicates that this deviation is perhaps an artefact of a combination of uncertainties related to transport characteristics and contact resistance but these effects are difficult to isolate in a complexly-coupled system such as a fuel cell. The level of qualitative agreement between numerical and experimental results is consistent with several previous analyses [49, 50]. Nevertheless, in order to investigate the capacity of the numerical model to fit the

experimental data, additional simulations were carried out considering all parameters the same except the porosity of the GDL, which was considered as $\epsilon_{GDL} = 0.4$ [26] in comparison to $\epsilon_{GDL} = 0.6$ listed in Table 3. It can be seen from Figure 3 that by only changing the porosity of the GDL, the polarization curve approaches the experimental results, demonstrating that the numerical results can fit the experimental data by tuning the parameters, which are not specified in Ref. [48]. The results shown in Section 3 corresponds to the physical properties and parameters listed in Table 3 because the qualitative nature of the results do not change as a result of changing ϵ_{GDL} from 0.6 to 0.4.

3. RESULTS & DISCUSSION

The model presented in this analysis is used to assess the influence of the flow direction in the flow channels on the overall fuel cell performance. In this paper, the co-flow configuration refers to the condition when the flows in the channels on both anode and cathode sides are in the same direction. By contrast, the flow direction in the channel on the cathode side is opposite to that in the channel on the anode side in the counter-flow configuration. A schematic representation of the different configurations is presented in Figure 4. Moreover, the effects of the operating temperature and the humidification of the gaseous mixture at the channel inlets for anion-exchange fuel cells have also been analysed. The operating parameters used in this study were taken from published literature and are presented in Table 6 [15].

3.1 Effect of flow direction

In order to investigate the effect of the flow direction on the fuel cell performance, three different temperature values have been considered for both co-flow and counter-flow configurations. The variation of voltage with current density for both co-flow and counter-flow configurations are shown in Figure 5, which demonstrates that for the set of parameters used, the flow direction in the channels does not a major influence on the overall performance of the fuel cell because the supply of reactant species to the catalyst layer is not affected by the flow direction for these operating conditions. Nevertheless, it has been found that the gradient of water vapour molar concentration is slightly higher in the counter-

flow configuration at the cathode side, mainly due to the slightly higher drag of liquid water from the anode side, which is consistent with previous findings [51].

3.2 Effect of operating temperature

As the flow direction does not have a major influence on the overall fuel-cell performance, the influence of operating temperature (which is the temperature at which the mixture is supplied) on the fuel cell performance has been analysed for the counter-flow configuration. Figure 6 shows that an increase in the operating temperature increases the mean current density for a given output voltage. An increase in operational temperature improves the electrochemical kinetics according to Eqs. 16 and 17. The hydration of the membrane play an important role in the fuel cell performance. Figure 7a demonstrates that the membrane water content increases with increasing temperature, which is in accordance with previous experimental findings [52]. Thus, the enhanced ion conductivity due to high water content in the membrane gives rise to a smaller Ohmic loss in the membrane. The product of the electrochemical reaction is water in the liquid phase in the anode catalyst layer. Figure 7b shows that the volume fraction of liquid water decreases as the temperature increases. Although the liquid water production increases for higher temperatures, this production is superseded by high evaporation rate at high-temperature values due to the fact that the saturation pressure in the catalyst and gas diffusion layers are higher than the water vapour pressure. Furthermore, the combination of high relative humidity at the anode side and the water production in the liquid phase are responsible to the back diffusion process which drags liquid water from the anode to the cathode side in the dissolved phase. This, in turn, contributes to the decrease of the liquid water fraction in the anode side and also enhances the hydration of the membrane and catalyst layer in the cathode side.

3.3 Effect of inlet humidification

Figure 8 shows that the relative humidity of the supplied mixture at the inlets has a significant influence on the fuel cell performance. The water demand for OH^- formation is directly related to the elevation of the Butler-Volmer reaction rate. Thus, the relative humidity has a higher impact in the lower output voltages where the current density values are high. A decrease in relative humidity from 90% to 80% shows a more drastic loss of performance that that is observed when the relative humidity is decreased from 100% to 90%. The extent of dehydration of membrane is much greater when the relative humidity

drops from 90% to 80% than the corresponding effect as a result of the relative humidity drop from 100% to 90%. Since the sorption and desorption processes are governed by the gradient of water activity between the anode and cathode side, the hydration of the membrane is negatively affected by a reduction of relative humidity at the channel inlets, which gives rise to higher ionic resistivity (i.e. higher ohmic loss) leading to a smaller value of current density than better hydrated cases. Therefore, the membrane water content reduces with the weakening of water transfer within the membrane, which can be substantiated from Figure 9a. Regarding the liquid water phase, as presented in the Figure 9b, the liquid water fraction is higher for the better humidified case. The main reason for the reduction of the liquid water fraction within the catalyst and gas diffusion layers is the fact that the lower relative humidity enhances the evaporation processes. In addition to that, as the overall performance of the fuel cell is compromised by a less hydrated membrane state, the water produced due to the electrochemical reaction is partially dragged from the anode catalyst layer to the membrane in order to compensate the dehydrated condition caused by the decrease in the relative humidity at the flow channel inlet. Moreover, the relative humidity has also an impact in the heat transport within the layers. A larger gradient of molar water concentration across the layers (vertical mid-plane) is observed for the values of smaller relative humidity, resulting in the extraction of more latent heat from the surface. Heat generation within the fuel cell due to the hydrogen oxidation reaction (HOR), which in turn affects the local current density due to its temperature dependence. Therefore, the equilibrium between temperature and reaction rate is altered and a negative feedback between temperature and current density is obtained as shown in Figure 10a. Thus, when combining the smaller heat generation due to the smaller current density and the extraction of latent heat from the surface, the temperature for lower relative humidity is observed to be smaller than the higher relative humidity cases, as shown in Figure 10b.

4. CONCLUSIONS

A three-dimensional numerical model has been used to analyse the influences of the flow mode, operating temperature and relative humidity on a single channel anion exchange membrane fuel cell performance. The overall performance of the AEM fuel cell has not been significantly affected by the flow direction in the channels for the operating parameters considered in this study. Nevertheless, the

overall performance of the AEM fuel cell has been found to be significantly affected by the operating temperature and relative humidity. An increase in operating temperature has a positive influence on the overall performance of the fuel cell due to the enhancement of the electrochemical kinetics and also because of the better hydration condition of the membrane. The relative humidity, when decreased, adversely affects the performance of the fuel cell, mainly due to the high resistance offered to the ions to diffuse in a poor hydration membrane environment. Moreover, the lower relative humidity cases exhibit lower local temperatures, which also contribute to the reduction of the average current density produced in the fuel cell.

ACKNOWLEDGEMENTS

The financial support of CAPES (the Science without Borders Project) through the grant n. BEX / 13011-13-8 is gratefully acknowledged. Dr. Mohamed Mamlouk from Newcastle University is also gratefully acknowledged for the support he provided during the preparation of this manuscript.

REFERENCES

[1] Siegel C. Review of computational heat and mass transfer modeling in polymer-electrolyte-membrane (PEM) fuel cells. Energy. 2008;33:1331-52.
[2] Wang YJ, Qiao JL, Baker R, Zhang JJ. Alkaline polymer electrolyte membranes for fuel cell applications. Chemical Society Reviews. 2013;42:5768-87.
[3] Office of Energy & Renewable Energy. 2016.
[4] Page K, Rowe B. An overview of polymer electrolyte membranes for fuel cell applications. Polymers for Energy Storage and Delivery: Polyelectrolytes for Batteries and Fuel Cells. 2012;1096:147-64.
[5] Borup R, Meyers J, Pivovar B, Kim YS, Mukundan R, Garland N, et al. Scientific aspects of polymer electrolyte fuel cell durability and degradation. Chemical Reviews. 2007;107:3904-51.
[6] Mehta V, Cooper JS. Review and analysis of PEM fuel cell design and manufacturing. Journal of Power Sources. 2003;114:32-53.
[7] Das PK, Li X, Liu ZS. Analysis of liquid water transport in cathode catalyst layer of PEM fuel cells. Int J Hydrogen Energ. 2010;35:2403-16.
[8] Das PK, Li X, Xie Z, Liu ZS. Effects of catalyst layer structure and wettability on liquid water transport in polymer electrolyte membrane fuel cell. Int J Energ Res. 2011;35:1325-39.
[9] Xing L, Mamlouk M, Scott K. A two dimensional agglomerate model for a proton exchange membrane fuel cell. Energy. 2013;61:196-210.
[10] Cetinbas FC, Advani SG, Prasad AK. An Improved Agglomerate Model for the PEM Catalyst Layer with Accurate Effective Surface Area Calculation Based on the Sphere-Packing Approach. Journal of the Electrochemical Society. 2014;161:F803-F13.
[11] Das PK, Weber AZ. Water Management in PEMFC with Ultra-Thin Catalyst-Layers. Proceedings of the Asme 11th Fuel Cell Science, Engineering, and Technology Conference, 2013. 2014.
[12] Weber AZ, Borup RL, Darling RM, Das PK, Dursch TJ, Gu WB, et al. A Critical Review of Modeling Transport Phenomena in Polymer-Electrolyte Fuel Cells. Journal of the Electrochemical Society. 2014;161:F1254-F99.
[13] Zenyuk IV, Das PK, Weber AZ. Understanding Impacts of Catalyst-Layer Thickness on Fuel-Cell Performance via Mathematical Modeling. Journal of the Electrochemical Society. 2016;163:F691-F703.
[14] Deng H, Huo S, Chang YF, Zhou YB, Jiao K. Transient analysis of alkaline anion exchange membrane fuel cell anode. Int J Hydrogen Energ. 2013;38:6509-25.
[15] Jiao K, He P, Du Q, Yin Y. Three-dimensional multiphase modeling of alkaline anion exchange membrane fuel cell. Int J Hydrogen Energ. 2014;39:5981-95.
[16] Huo S, Deng H, Chang YF, Jiao K. Water management in alkaline anion exchange membrane fuel cell anode. Int J Hydrogen Energ. 2012;37:18389-402.
[17] Li H, Tang YH, Wang ZW, Shi Z, Wu SH, Song DT, et al. A review of water flooding issues in the proton exchange membrane fuel cell. Journal of Power Sources. 2008;178:103-17.
[18] Duan Q, Ge S, Wang C-Y. Water uptake, ionic conductivity and swelling properties of anion-exchange membrane. Journal of Power Sources. 2013;243:773-8.
[19] Malko D, Lopes T, Ticianelli EA, Kucernak A. A catalyst layer optimisation approach using electrochemical impedance spectroscopy for PEM fuel cells operated with pyrolysed transition metal-N-C catalysts. Journal of Power Sources. 2016;323:189-200.
[20] Li Z, Shao M, Zhou L, Yang Q, Zhang C, Wei M, et al. Carbon-based electrocatalyst derived from bimetallic metal-organic framework arrays for high performance oxygen reduction. Nano Energy. 2016;25:100-9.
[21] Ting-Wei H, Hamza Q, Guan-Ren L, Szu-yuan C, Chung-Jen T. Production of high-performance and improved-durability Pt-catalyst /support for proton-exchange-membrane fuel cells with pulsed laser deposition. Journal of Physics D: Applied Physics. 2016;49:255601.
[22] Mamlouk M, Scott K, Horsfall JA, Williams C. The effect of electrode parameters on the performance of anion exchange polymer membrane fuel cells. Int J Hydrogen Energ. 2011;36:7191-8.
[23] Das PK, Li X, Liu ZS. Analytical approach to polymer electrolyte membrane fuel cell performance and optimization. Journal of Electroanalytical Chemistry. 2007;604:72-90.

[24] Mamlouk M, Kumar SMS, Gouerec P, Scott K. Electrochemical and fuel cell evaluation of Co based catalyst for oxygen reduction in anion exchange polymer membrane fuel cells. Journal of Power Sources. 2011;196:7594-600.
[25] Sohn YJ, Choi JI, Kim K. Numerical Analysis on Water Transport in Alkaline Anion Exchange Membrane Fuel Cells. Electrochemistry. 2015;83:80-3.
[26] Peng SK, Gong J, Xu X, Sui PC, Lu SF, Xiang Y. Numerical and Experimental Analyses on Deviated Concentration Loss with Alkaline Anion-Exchange Membrane Fuel Cells. J Phys Chem C. 2015;119:24276-81.
[27] Berg P, Promislow K, St Pierre J, Stumper J, Wetton B. Water management in PEM fuel cells. Journal of the Electrochemical Society. 2004;151:A341-A53.
[28] Wu H, Li XG, Berg P. On the modeling of water transport in polymer electrolyte membrane fuel cells. Electrochim Acta. 2009;54:6913-27.
[29] Ge SH, Yi BL. A mathematical model for PEMFC in different flow modes. Journal of Power Sources. 2003;124:1-11.
[30] Deng H, Wang DW, Xie X, Zhou YB, Yin Y, Du Q, et al. Modeling of hydrogen alkaline membrane fuel cell with interfacial effect and water management optimization. Renew Energ. 2016;91:166-77.
[31] Li YS, Zhao TS. Ultra-low catalyst loading cathode electrode for anion-exchange membrane fuel cells. Int J Hydrogen Energ. 2012;37:15334-8.
[32] Deng H, Wang D, Wang R, Xie X, Yin Y, Du Q, et al. Effect of electrode design and operating condition on performance of hydrogen alkaline membrane fuel cell. Applied Energy. 2016;183:1272-8.
[33] Sommer EM, Vargas JVC, Martins LS, Ordonez JC. The maximization of an alkaline membrane fuel cell (AMFC) net power output. Int J Energ Res. 2016;40:924-39.
[34] Bruggeman DAG. Berechnung verschiedener physikalischer Konstanten von heterogenen Substanzen. I. Dielektrizitätskonstanten und Leitfähigkeiten der Mischkörper aus isotropen Substanzen. Annalen der Physik. 1935;416:636–64.
[35] Das PK, Li X, Liu ZS. Effective transport coefficients in PEM fuel cell catalyst and gas diffusion layers: Beyond Bruggeman approximation. Applied Energy. 2010;87:2785-96.
[36] Liu XL, Lou GF, Wen Z. Three-dimensional two-phase flow model of proton exchange membrane fuel cell with parallel gas distributors. Journal of Power Sources. 2010;195:2764-73.
[37] Udell KS. Heat-Transfer in Porous-Media Considering Phase-Change and Capillarity - the Heat Pipe Effect. International Journal of Heat and Mass Transfer. 1985;28:485-95.
[38] Das PK, Santamaria AD, Weber AZ. Interactions between liquid-water and gas-diffusion layers in polymer-electrolyte fuel cells. Procedia Engineering. 2015;105:751-6.
[39] Das PK, Grippin A, Kwong A, Weber AZ. Liquid-Water-Droplet Adhesion-Force Measurements on Fresh and Aged Fuel-Cell Gas-Diffusion Layers. Journal of the Electrochemical Society. 2012;159:B489-B96.
[40] Santamaria AD, Das PK, MacDonald JC, Weber AZ. Liquid-Water Interactions with Gas-Diffusion-Layer Surfaces. Journal of the Electrochemical Society. 2014;161:F1184-F93.
[41] Weber AZ, Newman J. Modeling transport in polymer-electrolyte fuel cells. Chemical Reviews. 2004;104:4679-726.
[42] Ye Q, Van Nguyen T. Three-dimensional simulation of liquid water distribution in a PEMFC with experimentally measured capillary functions. Journal of the Electrochemical Society. 2007;154:B1242-B51.
[43] Springer TE, Zawodzinski TA, Gottesfeld S. Polymer Electrolyte Fuel-Cell Model. Journal of the Electrochemical Society. 1991;138:2334-42.
[44] Das PK, Li X, Liu ZS. A three-dimensional agglomerate model for the cathode catalyst layer of PEM fuel cells. Journal of Power Sources. 2008;179:186-99.
[45] Manual FU. Fluent Inc. 2015.
[46] Xing L, Liu XT, Alaje T, Kumar R, Mamlouk M, Scott K. A two-phase flow and non-isothermal agglomerate model for a proton exchange membrane (PEM) fuel cell. Energy. 2014;73:618-34.
[47] Patankar S. Numerical heat transfer and fluid flow: CRC press; 1980.
[48] Kruusenberg I, Matisen L, Shah Q, Kannan AM, Tammeveski K. Non-platinum cathode catalysts for alkaline membrane fuel cells. Int J Hydrogen Energ. 2012;37:4406-12.

[49] Kwac LK, Kim HG. Investigation of gas flow characteristics in proton exchange membrane fuel cell. Journal of Mechanical Science and Technology. 2008;22:1561-7.
[50] Wu H. Mathematical modeling of transient transport phenomena in PEM fuel cells. 2009.
[51] Mishler J, Wang Y, Mukundan R, Spendelow J, Hussey DS, Jacobson DL, et al. Probing the water content in polymer electrolyte fuel cells using neutron radiography. Electrochim Acta. 2012;75:1-10.
[52] Li YS, Zhao TS, Yang WW. Measurements of water uptake and transport properties in anion-exchange membranes. Int J Hydrogen Energ. 2010;35:5656-65.

TABLE CAPTIONS

Table 1 – List of transport parameters [15]

Table 2 –List of electrochemical kinetics parameters [36]

Table 3 – List of structural parameters [15]

Table 4 – List of physical properties [50]

Table 5 – Mesh independence – Effect of N^x, N^y and N^z on the error of the average current density and the non-dimensional minimum cell distance (i.e. $\emptyset = \Delta_{min,cell}/L$ where L is the largest dimension in the direction in question) and grid expansion ratio (r) values for the M5 mesh.

Table 6 – List of operating parameters [15]

TABLES

Table 1 – List of transport parameters [15]

Parameter	**Correlation**	**Unit**
Hydrogen dynamic viscosity, T(K)	$\mu_{H_2} = 3.205\text{x}10^{-5}\left(\frac{T}{293.85}\right)^{1.5}(T+72.0)^{-1.0}$	(kg/m·s)
Oxygen dynamic viscosity, T(K)	$\mu_{O_2} = 8.46\text{x}10^{-3}\left(\frac{T}{292.25}\right)^{1.5}(T+127.0)^{-1.0}$	(kg/m·s)
Water vapour dynamic viscosity, T(K)	$\mu_{H_2O,g} = 7.512\text{x}10^{-3}\left(\frac{T}{291.15}\right)^{1.5}(T+120.0)^{-1.0}$	(kg/m·s)
Hydrogen diffusivity, T(K), P(Pa)	$D_{H_2} = 1.055\text{x}10^{-4}\left(\frac{T}{333.15}\right)\left(\frac{101325.0}{P}\right)$	(m^2/s)
Oxygen diffusivity, T(K), P(Pa)	$D_{O_2} = 2.652\text{x}10^{-4}\left(\frac{T}{333.15}\right)\left(\frac{101325.0}{P}\right)$	(m^2/s)
Water vapour diffusivity, T(K), P(Pa)	$D_{H_2O,g} = 2.982\text{x}10^{-5}\left(\frac{T}{333.15}\right)\left(\frac{101325.0}{P}\right)$	(m^2/s)

Table 2 –List of electrochemical kinetics parameters [36]

Properties	**Value**	**Unit**
Exchange current density multiply specific reactive surface area, anode, $A_s j_{0,a}$	2.0×10^8	(A/m^3)
Exchange current density multiply specific reactive surface area, cathode, $A_s j_{0,c}$	1.62×10^2	(A/m^3)
Reference hydrogen concentration, $C_{H_2}^{ref}$	0.0564	($kmol/m^3$)
Reference oxygen concentration, $C_{O_2}^{ref}$	0.00339	($kmol/m^3$)
Anodic transfer coefficient, α_a	0.5	
Anodic transfer coefficient, α_c	0.5	

Table 3 – List of structural parameters [15]

Parameter	**Value**	**Unit**
Thickness of GDL, δ_{GDL}	2.0×10^{-4}	(m)
Thickness of CL, δ_{CL}	1.0×10^{-5}	(m)
Thickness of membrane, δ_{mem}	2.8×10^{-5}	(m)
Channel length, l	0.1	(m)
Channel width, w_c	5.0×10^{-4}	(m)
Channel height, h	1.0×10^{-3}	(m)
Rib width, w_r	5.0×10^{-4}	(m)
Intrinsic permeability of CL, K_{CL}^0	6.2×10^{-13}	(m^2)
Intrinsic permeability of GDL, K_{GDL}^0	6.2×10^{-12}	(m^2)
Porosities of GDL, ϵ_{GDL}	0.6	
Porosities of CL, ϵ_{CL}	0.3	
Volume fraction of ionomer, ω	0.22	

Table 4 – List of physical properties [50]

Parameter	**Value**	**Unit**
Thermal conductivity of CL, k_{CL}	1.0	(W/m·K)
Thermal conductivity of GDL, k_{GDL}	1.0	(W/m·K)
Thermal conductivity of membrane, k_{mem}	0.95	(W/m·K)
Thermal conductivity of BP, k_{BP}	20.0	(W/m·K)
Thermal conductivity of hydrogen, k_{H_2}	0.204	(W/m·K)
Thermal conductivity of air, k_{air}	0.03	(W/m·K)
Thermal conductivity of water vapour, $k_{H_2O,g}$	0.023	(W/m·K)
Thermal conductivity of liquid water, $k_{H_2O,l}$	0.67	(W/m·K)
Specific heat of CL, $C_{p,CL}$	3300.0	(J/kg·K)
Specific heat of GDL, $C_{p,GDL}$	568.0	(J/kg·K)
Specific heat of membrane, $C_{p,mem}$	833.0	(J/kg·K)
Specific heat of BP, $C_{p,BP}$	1580.0	(J/kg·K)
Liquid water density, ρ_l	970.0	(kg/m^3)
Contact angle, θ	100	(°)
Dry density membrane, ρ_{mem}	1092.7	(kg/m$^{3)}$
Equivalent weight, EW	588.24	(kg/kmol)
Evaporation/Condensation rates, $\gamma_{evap,cond}$	100.0	(1/s)
Sorption/Desorption rates, ζ_{mem}	1.0	(1/s)
Entropy change of reaction in anode, ΔS	163303.5	(J/kmol·K)
Condensation latent heat, h_{cond}	2.395x10^6	(J/kg)

Table 5 – Mesh independence – Effect of N^x, N^y and N^z on the error of the average current density and the non-dimensional minimum cell distance (i.e. $\emptyset = \Delta_{min,cell}/L$ where L is the largest dimension in the direction in question) and grid expansion ratio (r) values for the M5 mesh.

	N^x	N^y	N^z		N^x	N^y	N^z		N^x	N^y	N^z
M1	8	10	100	**M4**	10	10	100	**M7**	10	10	80
M2	10			**M5**		15		**M8**			100
M3	12			**M6**		20		**M9**			120

	Err^x (%)		Err^y (%)		Err^z (%)
M1	2.37	**M4**	6.85	**M7**	3.79
M2	1.29	**M5**	3.94	**M8**	1.74
M3	1.13	**M6**	1.24	**M9**	0.93

	$\emptyset_x$	$\emptyset_y$	$\emptyset_z$	r_x	r_y	r_z
Bipolar plate	0.1	2.643×10^{-5}	0.01	1	1.211	1
Flow channel		2.643×10^{-5}			1.211	
Gas diffusion layer		5.286×10^{-6}			1.211	
Catalyst layer		2.643×10^{-7}			1.211	
Membrane		7.400×10^{-7}			1.211	

Table 6 – List of operating parameters [15]

Parameter	**Value**	**Unit**
Operating temperature, T_0	313.15, 318.15, 323.15 (base case), 328.15, 333.15	(K)
Relativity humidity at anode, RH_a	100 (base case), 90, 80, 70, 50	(%)
Relativity humidity at cathode, RH_c	100 (base case), 90, 80, 70, 50	(%)
Output voltage, V_{out}	1.0, 0.9, 0.8, 0.7, 0.6, 0.5 (base case), 0.4, 0.3	(V)
Stoichiometry ratio at anode, ξ_a	2.0	
Stoichiometry ratio at cathode, ξ_c	3.0	

FIGURE CAPTIONS

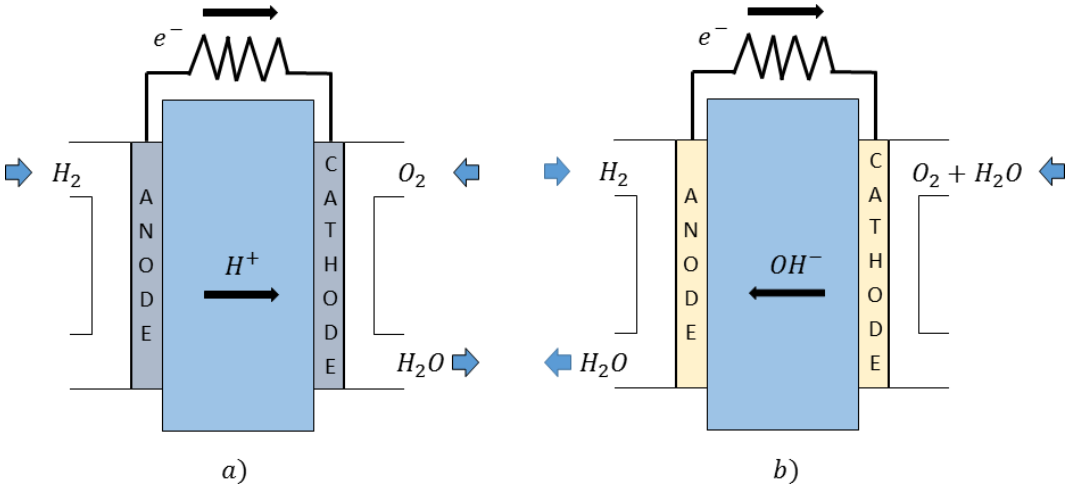

Figure 1 - Schematic representation of PEM and AEM

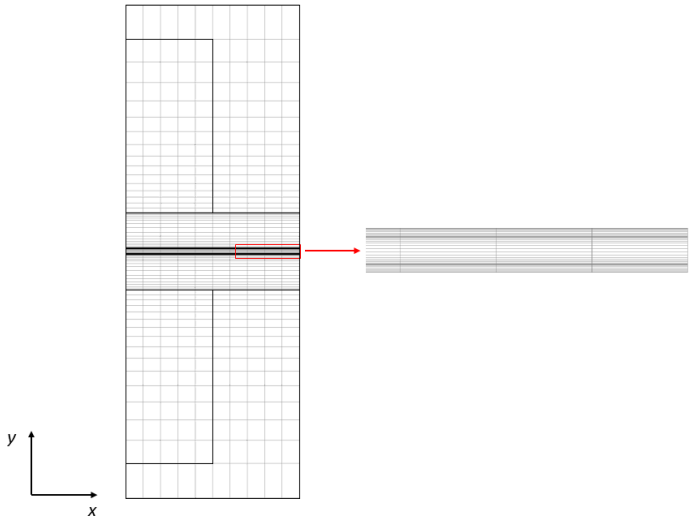

Figure 2 - Representation of the computational domain

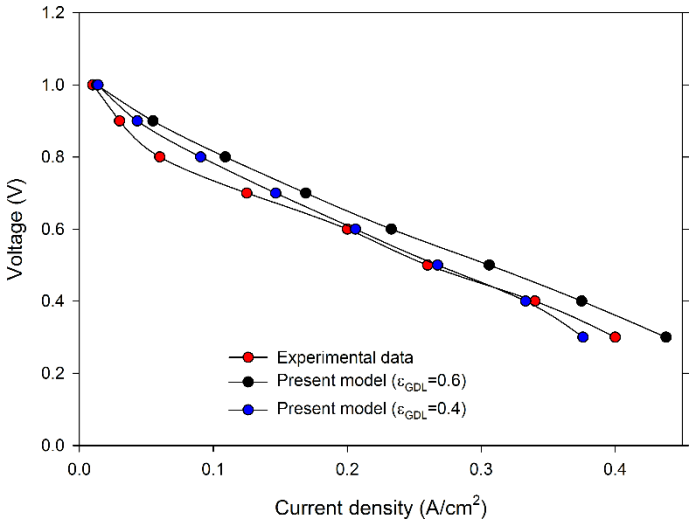

Figure 3 – Model validation: polarisation curve [48]

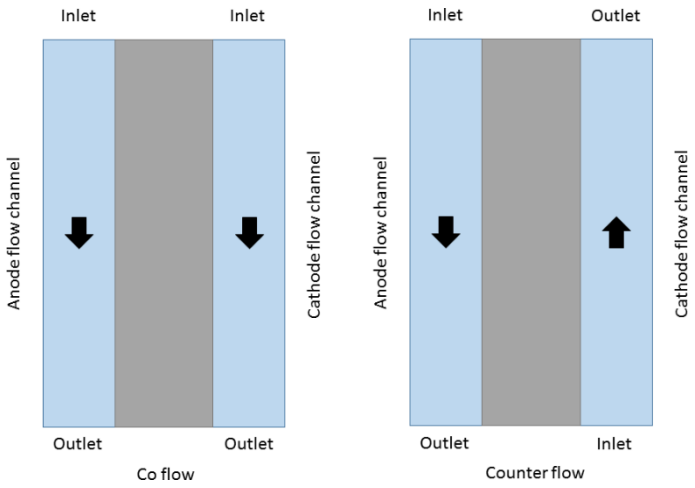

Figure 4 – Flow configuration: co-flow and counter-flow

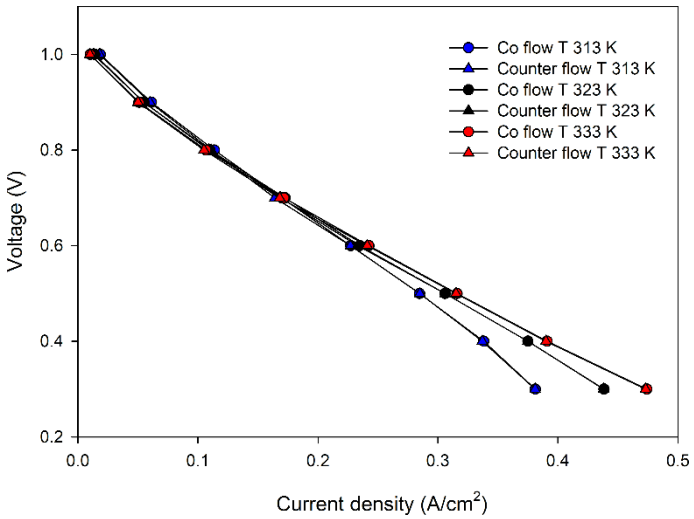

Figure 5 – Co-flow and counter-flow polarisation curve comparison

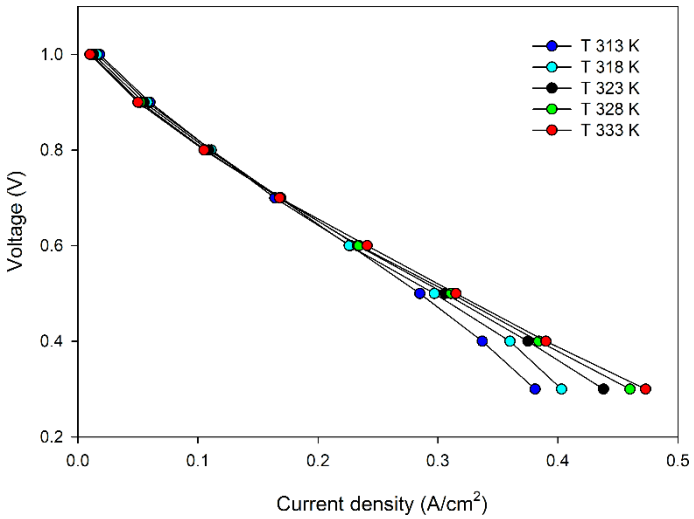

Figure 6 – Polarisation curve: effect of operational temperature on the fuel cell performance

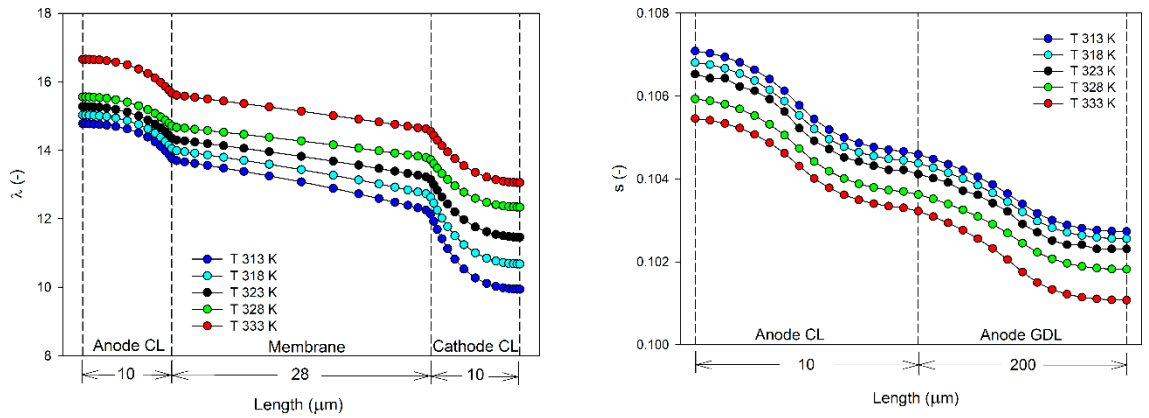

a) b)

Figure 7 – Effect of operational temperature on: a) liquid water fraction b) membrane water content

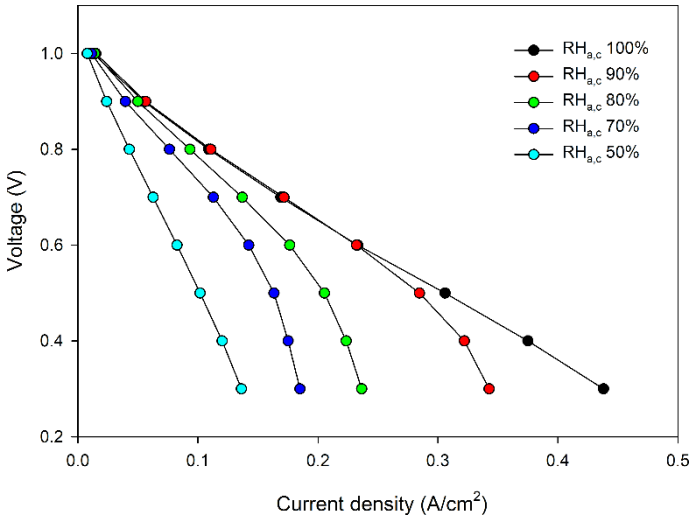

Figure 8 – Polarisation curve: effect of inlet relativity humidity on the fuel cell performance

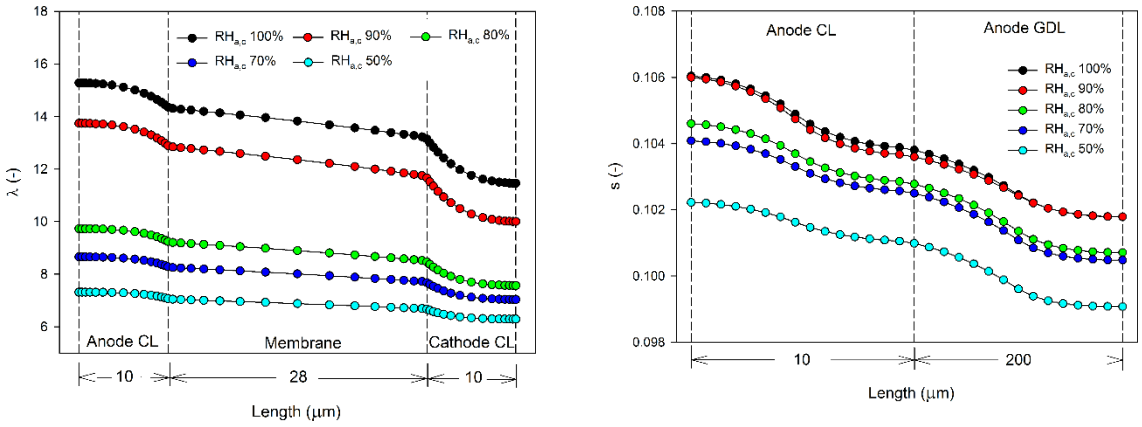

a) b)

Figure 9 – Effect of inlet relativity humidity on: a) liquid water fraction b) membrane water content

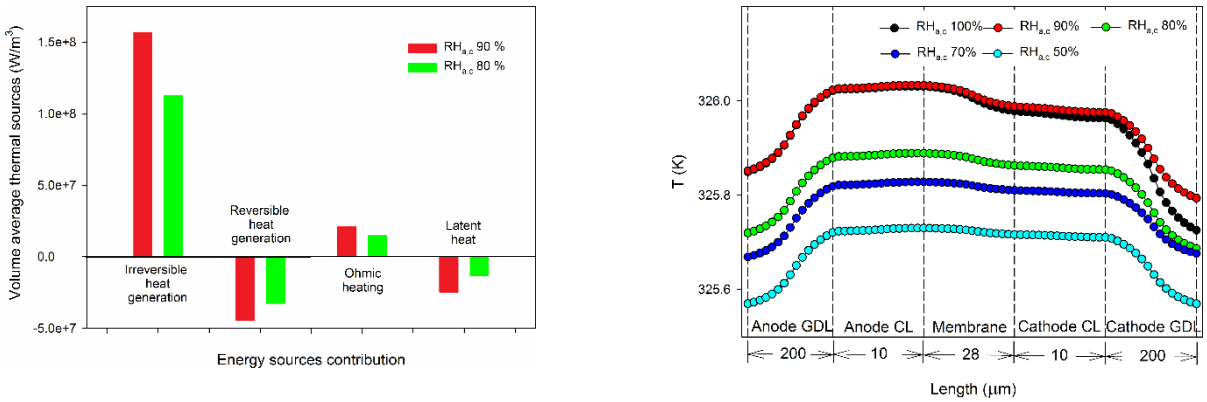

a) b)

Figure 10 – a) Energy source contribution for different relative humidity cases b) Effect of relative humidity on the temperature profile